This article has been accepted for inclusion in a future issue of this journal. Content is final as presented, with the exception of pagination.

Mode-Scheduled Hybrid Control of Magnetorheological-Assisted Robotic Joints for Improved Energy Efficiency and Disturbance Rejection

Zirui Chen, Erwin Ang Tien Yew, Yuekang Fu, Zhongyuan Kong, Liang Zhang, *Member, IEEE*, and Shuaishuai Sun

***Abstract*—Robotic joints driven by permanent-magnet synchronous motors (PMSMs) face a practical tension between high-bandwidth motion tracking and energy-efficient static load holding. This article develops a joint-embedded coordination framework that augments electromagnetic actuation with a parallel semi-active magnetorheological (MR) bearing, while preserving a standard position-reference interface to upper-level control. MR engagement and current allocation are scheduled internally via guarded mode transitions, enabling a low-drag baseline mode during motion, an MR-assisted quasi-static holding mode (hereafter, holding mode) for energy-efficient finite-capacity holding, and an MR damping mode for dissipating disturbance-induced transients. A real-time load estimate is used for both PMSM feedforward compensation and load-dependent MR holding-current allocation. Mode transitions are guarded by measured position, velocity, and reference-update conditions. After break-away, the last holding current is retained to provide dissipative MR assistance during recovery. Experiments on an integrated MR–motor prototype demonstrate that the proposed coordination reduces the 25-s sequence-averaged accounted power at 20 N·m by 87.3%. In the variable-load task, it reduces the integral absolute position error J_{IAE} by 37.1% relative to the motor-only load-torque-observer-based active-compensation baseline, while achieving the lowest accounted average power among the compared methods.**

***Index Terms*—Joint-level control, magnetorheological bearing, semi-active actuation.**

Received 9 March 2026; revised 28 June 2026; accepted 3 August 2026. This work was supported in part by the National Natural Science Foundation of China under Grant U21A20119, Grant 52105081, and Grant 62303002; in part by the Major Project of Anhui Province Science and Technology Innovation Breakthrough Plan under Grant 202423h08050003; in part by the Key R&D Program of Anhui Province under Grant 202104a05020009; in part by the USTC start-up funding under Grant KY2090000067; and in part by the Fundamental Research Funds for the Central Universities under Grant SC5290005162. *(Corresponding authors: Liang Zhang; Shuaishuai Sun.)*

Zirui Chen, Erwin Ang Tien Yew, Yuekang Fu, Zhongyuan Kong, and Shuaishuai Sun are with the CAS Key Laboratory of Mechanical Behavior and Design of Materials and Institute of Humanoid Robots, School of Engineering Sciences, University of Science and Technology of China, Hefei, Anhui 230026, China (e-mail: sssun@ustc.edu.cn).

Liang Zhang is with the School of Electrical Engineering and Automation, Anhui University, Hefei, Anhui 230601, China (e-mail: liangzhang@ahu.edu.cn).

Digital Object Identifier 10.1109/TIE.2026.3722995

I. Introduction

PERMANENT-MAGNET synchronous motors (PMSMs) are widely adopted in modern servo drives, supported by mature drive technology and fast-response position servo control [1], [2], [3]. In heavy-duty industrial servo axes and robotic joints with frequent quasi-static support [4], [5], [6], a single drive is often required to combine high-bandwidth tracking [1], [7] with near-zero-speed holding and impact/transient tolerance; however, holding incurs sustained torque current and continuous copper loss [8], while purely active transient disturbance rejection is limited by delay, noise, and saturation [9]. Accordingly, augmenting the joint/axis with an auxiliary holding/dissipation torque path has been actively explored in robotics and wearable systems [4], [10].

Magnetorheological (MR) devices offer a compact semi-active alternative: by modulating field-dependent yield stress, an MR element can generate controllable resistive torque and be packaged as brakes, clutches, or bearings [11], [12], [13], [14], [15]. Among these realizations, MR bearing implementations [10] are attractive for joint modules because they integrate coaxially as a compact parallel torque branch, and low off-state drag/transparency has been demonstrated in MR joint modules [10], which is desirable in collaborative and contact-rich robotic applications [4]. The pre-yield regime can support finite-capacity quasi-static holding, whereas the post-yield regime can dissipate transient kinetic energy, potentially reducing motor-side continuous current demand. Existing joint-level solutions address the holding–motion trade-off at different design layers: mechanical brakes/locks can provide low-power support but usually operate through discrete engagement and release [16], [17]; high-reduction and quasi-direct-drive actuators reshape the trade-off among reflected inertia, friction, backdrivability, and torque density [18], [19]; and impedance/admittance control improves interaction behavior, while static load support still relies on motor-side torque [20], [21]. The MR path is therefore introduced here as a complementary semi-active branch for finite-capacity holding and transient dissipation.

However, MR integration into high-performance servo loops is not plug-and-play. Prior work often focuses on hardware feasibility [13], [22] or hysteresis modeling/compensation [23], [24], leaving three practical gaps: (1) a joint-level, drive-compatible coordination policy is still underexplored, so MR engagement may be misaligned with servo objectives and become parasitic drag rather than an auxiliary torque pathway [4], [10]; (2) MR engagement is frequently implemented in a binary/constant-current manner that can degrade back-drivability and efficiency when not synchronized with servo objectives [24], [25]; and (3) hybrid behaviors are sometimes delegated to upper-level optimization (e.g., MPC), which increases computation and pushes mode constraints and safety logic to planners, weakening servo-module encapsulation [26], [27], [28]. Therefore, a joint-level drive-compatible coordination mechanism is required to schedule MR engagement and allocate excitation.

Motivated by the need for drive-compatible MR integration, this article develops an MR-assisted joint module that augments a PMSM with a parallel semi-active MR bearing torque path and coordinates its engagement under a standard position interface. The main contributions are:

1) *Data-Driven MR Bearing Torque Modeling*: An empirical constitutive map of the MR bearing is identified from systematic characterization data, yielding a compact torque surface versus excitation current and rotational speed for real-time current allocation.
2) *Hybrid MR–Motor Role Coordination*: A joint-internal scheduler coordinates PMSM tracking, finite-capacity MR-assisted holding, damping recovery, and guarded release using measured state/reference guards, while $\hat{T}_L$ is used for PMSM feedforward and load-dependent holding-current allocation. The MR branch is released during nominal tracking and used for holding or dissipation at the joint module, without upper-level mode scheduling or online optimization.
3) *Torque-Platform Validation*: Extensive experiments on a dedicated torque test platform validate the identified torque model and demonstrate energy-efficient holding and disturbance rejection enabled by the proposed coordination strategy.

II. System Design and Modeling

This section establishes the configuration and a control-oriented model of the proposed MR-assisted motor joint for the observer and joint-level coordination to follow. The module (hereafter, the *MR-motor joint*) integrates a standard PMSM actuation path with a parallel MR-bearing path at the joint. Its mechanical layout is adopted from existing MR-bearing planetary designs and is not claimed as a structural contribution [29]. The section proceeds by summarizing the MR operating modes and experimentally identified torque characteristics, recalling the PMSM model in the synchronous d–q frame, and augmenting the joint mechanics with a data-driven MR torque term.

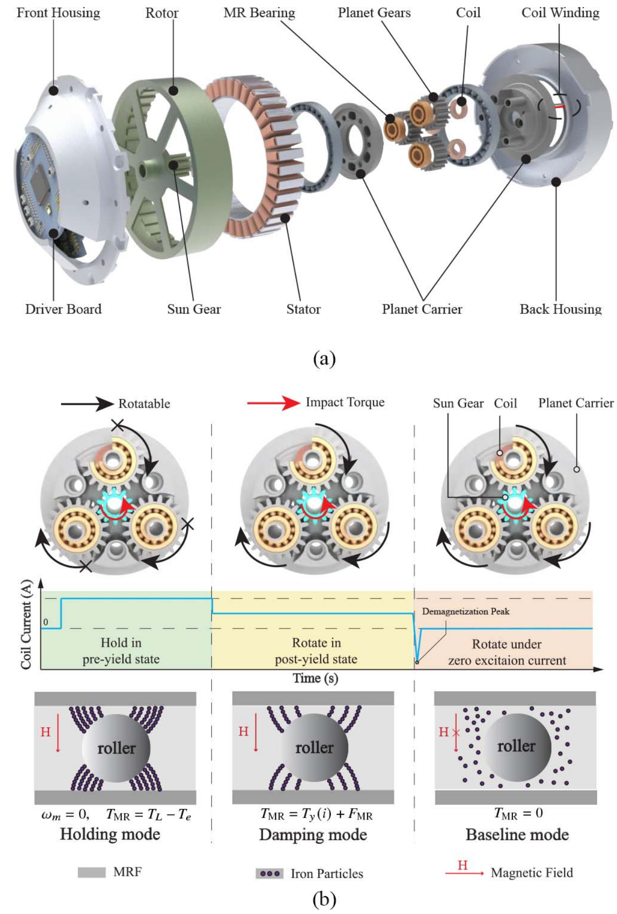

Fig. 1. MR-motor joint structure and MR-path operating regimes. (a) Mechanical layout. (b) MR regimes and coil-current profile.

A. Mechanical and Structural Overview of the MR Motor Joint

The MR-motor joint adds a semi-active MR torque path in parallel with a conventional PMSM drive [Fig. 1(a)]. Three MR bearings are mounted coaxially between the motor shaft and the output flange, establishing a parallel torque transmission path to the electromagnetic drive. The MR path is organized into three regimes according to the commanded coil current and the relative slip speed ω_m [Fig. 1(b)]. The brief negative-current segment in Fig. 1(b) is a release demagnetization pulse. It is used to accelerate the decay of remanent magnetization and is not considered a separate torque-producing mode. Unlike a conventional parking brake that mainly provides binary locking/release, the MR bearing is treated here as a regime-dependent semi-active torque element. *Baseline* de-energizes the coil ($i_{\mathrm{MR}} = 0$) to minimize drag so that the PMSM solely performs motion tracking. In MR-assisted quasi-static holding, the coil is excited to provide sufficient pre-yield capacity for sustaining the load within a small near-zero-speed region ($|\omega_m| \leq \omega_\epsilon$). The holding burden is then transferred mainly to the MR bearing, allowing the motor current to ramp down. This

TABLE I
MAIN HARDWARE AND ELECTRICAL PARAMETERS OF THE PMSM ACTUATOR AND MR PATH

Parameter	Value
Overall size and mass	$96.5\ \mathrm{mm} \times 92.5\ \mathrm{mm} \times 42.3\ \mathrm{mm}$; $\approx 0.53\ \mathrm{kg}$
Supply voltage and PMSM command limit	24 VDC supply used in experiments; output-side torque-command projected to $\lvert T^{\mathrm{cmd}}\rvert \le 22\ \mathrm{N \cdot m}$
Output torque and speed limits	$22\ \mathrm{N \cdot m}$ maximum output torque; $30\ \mathrm{rad/s}$ maximum output speed at 24 V supply
Torque constant and reduction ratio	$K_t = 0.63895\ \mathrm{N \cdot m/A}$ (output-side equivalent after $N_g = 6.33$)
Communication and sensing	high-speed 485, $4\ \mathrm{Mbit/s}$ baud rate, $6\ \mathrm{kHz}$ communication/control frequency, 15-bit absolute rotor encoder
MR-path electrical limit	$R_{\mathrm{coil}} \approx 4.6\ \Omega$, $0 \le i_{\mathrm{MR}} \le 1.5\ \mathrm{A}$; peak $-1.5\ \mathrm{A}$ demagnetization pulse within $50\ \mathrm{ms}$
Power/efficiency information used in this work	Energy comparison is based on measured current and resistance-based losses, not on standalone motor efficiency curves
Power accounting used in this work	measured-current Joule losses with $R_s = 0.21\ \Omega$

mode is referred to as holding for brevity. *Damping* keeps the MR interface in a rotating post-yield state so that the torque is strictly resistive

$$T_{\mathrm{MR}} = -\mathcal{F}_{\mathrm{MR}}(i_{\mathrm{MR}}, |\omega_m|)\,\mathrm{sgn}(\omega_m), \quad T_{\mathrm{MR}}\omega_m \le 0 \tag{1}$$

where $\mathcal{F}_{\mathrm{MR}}(\cdot)$ is identified as a current–speed torque map for real-time allocation.

Table I summarizes the main hardware and electrical parameters. In all energy comparisons, power is computed from measured currents and resistance-based Joule losses rather than from standalone motor efficiency curves.

B. Torque Modeling for Hybrid Coordination

This work relies on explicit MR torque maps for hybrid mode scheduling and current allocation: (1) the nominal quasi-static holding capacity $T_{\mathrm{hold}}(i_{\mathrm{MR}})$ at near-zero slip; and (2) the post-yield resistive surface $\mathcal{F}_{\mathrm{MR}}(i_{\mathrm{MR}}, |\omega_m|)$ during relative rotation. All model parameters are obtained via experimental identification and held-out validation (Section IV-A).

1) Quasi-Static Holding-Capacity Model: In this work, the static holding capacity is defined as the maximum load torque that can be sustained at near-zero slip without macroscopic break-away during the finite-duration characterization test. The measured T_{hold}–i_{MR} curve is monotone saturating, consistent with field-governed yield stress and magnetic saturation in MR media [11]; thus T_{hold} is parameterized by a four-parameter Hill model

$$T_{\mathrm{hold}}(i_{\mathrm{MR}}) = T_{\mathrm{res}} + (T_{\mathrm{sat}} - T_{\mathrm{res}})\frac{i_{\mathrm{MR}}^{n}}{k^{n} + i_{\mathrm{MR}}^{n}} \tag{2}$$

where T_{sat} denotes the saturated holding capacity, k is the offset-corrected half-saturation current, n shapes the transition steepness, and T_{res} captures the off-state offset (drag/residual friction). Here, $T_{\mathrm{hold}}(i_{\mathrm{MR}})$ denotes the maximum admissible quasi-static holding capacity rather than the instantaneous MR reaction torque.

2) Analytic Inverse for Minimum-Current Allocation: For energy-efficient holding, the minimum excitation current for a target holding torque is obtained by analytically inverting (2)

$$i_{\mathrm{req}}(T_{\mathrm{hold}}) = k\left(\frac{T_{\mathrm{hold}} - T_{\mathrm{res}}}{T_{\mathrm{sat}} - T_{\mathrm{hold}}}\right)^{\frac{1}{n}}. \tag{3}$$

The valid domain is $T_{\mathrm{hold}} \in (T_{\mathrm{res}}, T_{\mathrm{sat}})$. To avoid numerical amplification as $T_{\mathrm{hold}} \to T_{\mathrm{sat}}$, the commanded holding torque is bounded as

$$T_{\mathrm{cmd}} = \min\left(T_{\mathrm{hold}}, T_{\mathrm{sat}} - \delta_{\mathrm{sat}}\right), \qquad \delta_{\mathrm{sat}} > 0 \tag{4}$$

where δ_{sat} is introduced as a saturation guard to avoid ill-conditioned inverse allocation near the magnetic-saturation plateau. This guard is used only to avoid ill-conditioned inverse allocation near the saturation plateau; it is not intended to compensate hysteresis, thermal drift, or aging. The inverse map $i_{\mathrm{req}}(\cdot)$ is then evaluated using T_{cmd}.

3) Post-Yield Resistive Torque Model: Motivated by post-yield MR behavior [11], the resistive torque during relative rotation is modeled as an excitation-modulated yield-like term attenuated with slip speed, plus an off-state drag offset

$$\mathcal{F}_{\mathrm{MR}}(i_{\mathrm{MR}}, |\omega_m|) = T_y(i_{\mathrm{MR}})\, g(|\omega_m|) + T'_{\mathrm{res}} \tag{5}$$

with

$$T_y(i_{\mathrm{MR}}) = T'_{\mathrm{sat}}\frac{i_{\mathrm{MR}}^{n'}}{k'^{\,n'} + i_{\mathrm{MR}}^{n'}}, \qquad g(|\omega_m|) = e^{-\lambda|\omega_m|}. \tag{6}$$

C. Unified Joint Dynamics Modeling

The electrical dynamics of the PMSM in the synchronous d–q frame are [30]

$$\begin{aligned} u_d &= R_s i_d + L_d\frac{di_d}{dt} - \omega_e L_q i_q \\ u_q &= R_s i_q + L_q\frac{di_q}{dt} + \omega_e\left(L_d i_d + \psi_f\right) \end{aligned} \tag{7}$$

where symbols follow standard FOC notation, and p_n denotes the number of pole pairs. The motor-side electromagnetic torque is $T_{e,m} = (3/2)p_n\left[(L_d - L_q)i_d i_q + \psi_f i_q\right]$. Unless otherwise specified, T_e, T_L, and T_{MR} are expressed at the output side, with $T_e = N_g T_{e,m}$. Position, speed, and error signals reported in the experimental plots and tables are rotor-side encoder quantities unless explicitly labeled as output-side; output-side position errors are obtained by dividing rotor-side values by $N_g = 6.33$.

A unified mechanical equation that covers baseline and damping regimes is written as

$$J\dot{\omega}_m = T_e + T_{\mathrm{MR}} - T_L - B\omega_m \tag{8}$$

where J is the reflected inertia, B is the zero-field viscous friction, and T_L is the unknown external load torque. The MR torque is modeled as

$$T_{\mathrm{MR}} = \begin{cases} T_{\mathrm{res}}, & \text{Baseline (nominal)} \\ -\mathcal{F}_{\mathrm{MR}}(i_{\mathrm{MR}}, |\omega_m|)\,\mathrm{sgn}(\omega_m), & \text{Damping} \\ \mathrm{sat}\left(T_L - T_e,\, T_{\mathrm{hold}}(i_{\mathrm{MR}})\right), & \text{Holding} \end{cases} \tag{9}$$

where $\mathrm{sat}(x, T_{\max}) = \mathrm{sgn}(x)\min(|x|, T_{\max})$ enforces $|T_{\mathrm{MR}}| \leq T_{\mathrm{hold}}(i_{\mathrm{MR}})$. In baseline mode, $T_{\mathrm{MR}} \approx 0$: the residual off-state drag is not modeled as a fixed positive torque source, but is absorbed into the zero-field friction term and the bounded disturbance/modeling uncertainty used by the observer and stability analysis. The holding condition is valid when $i_{\mathrm{MR}} > 0$, $|\omega_m| \leq \omega_\epsilon$, and the required reaction torque remains within the available MR capacity. In a conservative form, this no-breakaway condition can be written as

$$|T_L - T_e| + \Delta_T \leq T_{\mathrm{hold}}(i_{\mathrm{MR}}) \tag{10}$$

where Δ_T accounts for load-estimation error, MR-map mismatch, sensor noise, and small load variations. The map $T_{\mathrm{hold}}(\cdot)$ is identified in (2).

Equations (8)–(9) provide a plant model for subsequent observer and controller design while explicitly reflecting the regime-dependent MR behavior.

III. Load-Aware Hybrid Coordination Framework

This section develops a hybrid coordination framework for the MR motor, where the PMSM and embedded MR bearing provide two coordinated actuation paths within a unified joint module. The coordinator preserves a standard position-control interface to upper-level controllers (i.e., the commanded reference remains θ_{ref}), while MR engagement and current allocation are handled internally based on load/disturbance awareness and measured motion states. Thus, the upper-level controller is not required to explicitly command braking, holding, or damping modes. Since the MR pathway is semi-active with distinct pre-yield quasi-static holding and post-yield dissipative behaviors, we adopt a mode-based policy with explicit constraint handling, which is more amenable to verification than continuously tuning an equivalent damping coefficient under hysteresis and magnetic saturation.

A. Design of Sliding-Mode Load Torque Observer

The sliding-mode observer (SMO) used for this estimate is referred to hereafter as the *SMO-based load-torque observer* (SMO-based LTO). Its output $\hat{T}_L$ provides load information for PMSM feedforward compensation and load-aware MR current allocation in the holding mode.

From the unified joint dynamics in (8), the unknown external load torque can be written as

$$T_L = T_e(i_q) + T_{\mathrm{MR}} - B\omega - J\dot{\omega}. \tag{11}$$

Direct evaluation of (11) is impractical because $\dot{\omega}$ is not directly measured and (J, B) as well as the MR torque map are subject to uncertainty. Therefore, we estimate T_L using a SMO that augments T_L as a state

$$\begin{cases} \dot{\hat{\omega}} = \dfrac{1}{J}\Big(T_e(i_q) + T_{\mathrm{MR}} - \hat{T}_L - B\hat{\omega}\Big) + k_1\ \mathrm{sgn}\left(\omega - \hat{\omega}\right) \\ \dot{\hat{T}}_L = -k_2\ \mathrm{sgn}\left(\omega - \hat{\omega}\right) \end{cases} \tag{12}$$

where $k_1, k_2 > 0$ are observer gains.

To make the effect of MR-model mismatch explicit, denote the true MR torque by $T_{\mathrm{MR}}^{\mathrm{true}}$ and define

$$e_{\mathrm{MR}} = T_{\mathrm{MR}}^{\mathrm{true}} - T_{\mathrm{MR}}. \tag{13}$$

Then the actual mechanical dynamics satisfy

$$J\dot{\omega} = T_e(i_q) + T_{\mathrm{MR}} + e_{\mathrm{MR}} - T_L - B\omega. \tag{14}$$

Define the estimation errors

$$e_\omega = \hat{\omega} - \omega, \qquad e_T = \hat{T}_L - T_L. \tag{15}$$

Combining (12) and (14) yields

$$\begin{cases} \dot{e}_\omega = -\dfrac{B}{J}e_\omega - \dfrac{1}{J}e_T - k_1\ \mathrm{sgn}(e_\omega) + d_\omega \\ \dot{e}_T = k_2\ \mathrm{sgn}(e_\omega) + d_T \end{cases} \tag{16}$$

where d_ω and d_T lump the effects of the signed MR-map mismatch contribution, parameter uncertainty, and load-torque variation.

Assumption 1: The lumped uncertainties are bounded, i.e., $|d_\omega(t)| \leq \bar{d}_\omega$ and $|d_T(t)| \leq \bar{d}_T$ for some finite constants. Moreover, the augmented torque error remains bounded during the reaching phase, i.e., $|e_T(t)| \leq \bar{e}_T$ for $t \in [0, t_r]$.

Let the sliding surface be $s = e_\omega$ and $V = (1/2)s^2$. From (16)

$$\begin{aligned} \dot{V} &= -\frac{B}{J}s^2 - \frac{1}{J}s\, e_T - k_1|s| + s\, d_\omega \\ &\leq -\frac{B}{J}s^2 - \Big(k_1 - \frac{\bar{e}_T}{J} - \bar{d}_\omega\Big)|s|. \end{aligned} \tag{17}$$

Thus, choosing $k_1 > (\bar{e}_T/J) + \bar{d}_\omega$ yields $\dot{V} \leq -\alpha\sqrt{2V}$ with $\alpha := k_1 - (\bar{e}_T/J) - \bar{d}_\omega > 0$, which guarantees finite-time reaching to $s = 0$ in the ideal case and to a small boundary layer in the presence of noise. In implementation, $\mathrm{sgn}(\cdot)$ is replaced by a saturation function to mitigate chattering, and (k_1, k_2) are selected conservatively based on observed modeling mismatch and measurement noise.

Finally, the SMO is intended for dynamically informative conditions (baseline or damping modes) where the joint motion excites (14). In the quasi-static holding regime, $\omega \approx 0$ and $J\dot{\omega} \approx 0$, so the measurements provide insufficient excitation to update T_L reliably. Accordingly, the most recent estimate $\hat{T}_L$ obtained during motion is held during holding and refreshed once the joint re-enters a dynamically excited mode.

B. Mode-Scheduled MR–Motor Role Coordination and Load-Aware Current Allocation

The MR-motor joint tracks θ_{ref} under unknown loading while reducing holding energy and dissipating transients. As shown in Fig. 2(a), the PMSM and MR bearing form two parallel torque paths coordinated by $\hat{T}_L$ and measured motion states. The coordinator selects among baseline, holding, and damping modes, disables load-estimate updating during near-zero-speed holding, and re-enables observation after break-away. Motor-copper and MR-coil losses are then evaluated using the same resistance-based accounting in the experiments.

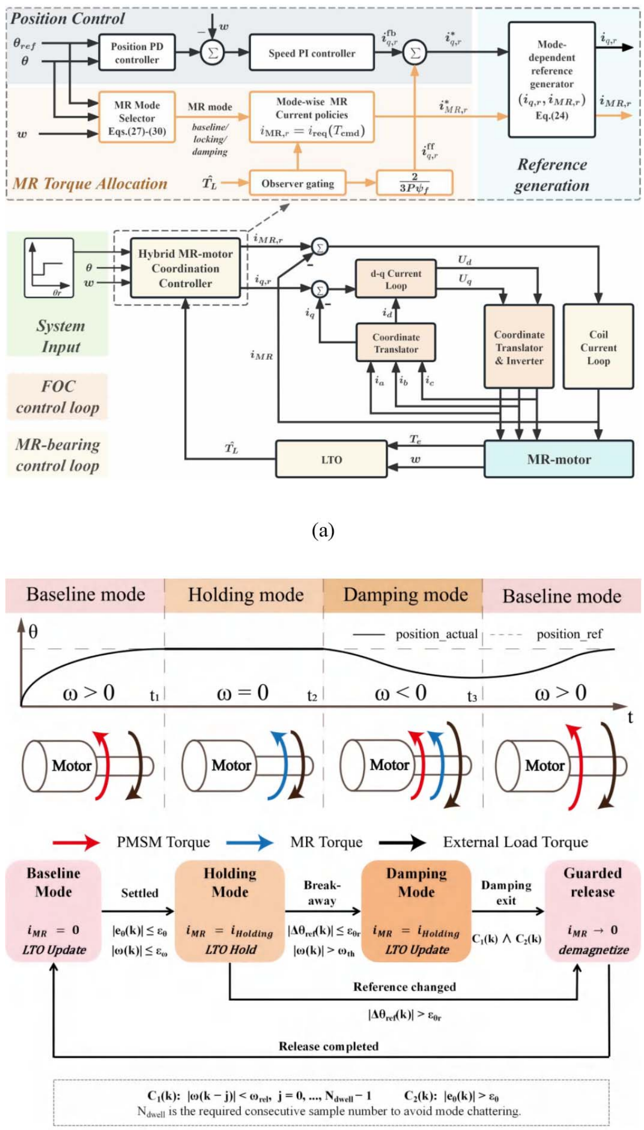

(a)

(b)

Fig. 2. Joint-level MR–motor coordination architecture and mode scheduler. (a) Overall architecture with expanded joint-level coordination logic for the MR–motor joint. (b) Illustration of mode transitions during a typical task.

1) Hybrid Formulation and Reference Generation: Define

$$e_\theta(k) := \theta_{\text{ref}}(k) - \theta(k), \quad \Delta\theta_{\text{ref}}(k) := \theta_{\text{ref}}(k) - \theta_{\text{ref}}(k-1)$$
$$x(k) := \begin{bmatrix} \theta(k) \\ \omega(k) \end{bmatrix}, \qquad u(k) := \begin{bmatrix} i_{q,r}(k) \\ i_{\text{MR},r}(k) \end{bmatrix}.$$

The cooperative controller is written as the hybrid law

$$u(k) = \mathcal{U}_{\sigma(k)}\big(x(k), \hat{T}_L(k)\big) \tag{18}$$

where $\sigma(k) \in \{\text{baseline}, \text{holding}, \text{damping}\}$ is selected internally from $(e_\theta, \Delta\theta_{\text{ref}}, \omega)$ and $\mathcal{U}_\sigma(\cdot)$ is the mode-wise policy. Guarded release is a transition routine; regular MR commands are nonnegative, and the release-only reverse pulse is defined in (29). Commands are projected onto admissible sets before driver output, e.g.,

$$\mathcal{S}_m := \{\, T_m^{\text{cmd}} : |T_m^{\text{cmd}}| \le 22\,\text{N m}\,\}$$
$$\mathcal{S}_{\text{MR}} := \{\, i_{\text{MR}} : 0 \le i_{\text{MR}} \le i_{\text{MR,max}}\}.$$

Here $\Pi_{\mathcal{S}}(\cdot)$ denotes projection; PMSM commands are torque-projected, whereas MR commands are current-projected.

Using the load-torque estimate $\hat{T}_L$, the q-axis feedforward current is computed as

$$i_{q,r}^{\text{ff}} = \frac{\hat{T}_L}{K_t}, \qquad K_t := N_g \frac{3}{2} p_n \psi_f \tag{19}$$

where $N_g = 6.33$ is the reduction ratio, p_n is the number of pole pairs, and ψ_f is the permanent-magnet flux linkage (with $i_d \approx 0$). The PMSM current reference is

$$i_{q,r}^{\star} = i_{q,r}^{\text{fb}} + i_{q,r}^{\text{ff}} \tag{20}$$

where $i_{q,r}^{\text{fb}}$ is generated by the PMSM tracking loop in Fig. 2(a). In parallel, an MR reference $i_{\text{MR},r}^{\star}$ is generated according to the selected mode and mapped via the inverse MR model. A mode-dependent reference generator then applies the PMSM output-side torque-command projection and MR-current projection to satisfy actuator limits and semi-active constraints, yielding the realizable commands for the inner loops.

2) Mode Selection and Guarded Transitions: Fig. 2(b) summarizes the three torque-producing states: reference updates trigger commanded guarded release, holding break-away triggers damping, and damping exits after dwell-confirmed low-speed detection.

The mode selection is implemented by the following guards. The controller enters holding when

$$|e_\theta(k)| \le \varepsilon_\theta, \qquad |\omega(k)| \le \varepsilon_\omega$$
$$|\Delta\theta_{\text{ref}}(k)| \le \varepsilon_{\theta_r}. \tag{21}$$

The three thresholds are the in-position, near-zero-speed, and reference-update guards.

If the reference changes

$$|\Delta\theta_{\text{ref}}(k)| > \varepsilon_{\theta_r} \tag{22}$$

guarded release is executed before baseline tracking. A reference update is treated as commanded motion; therefore, guarded release is executed immediately rather than after dwell confirmation.

If the reference is unchanged and

$$|\omega(k)| > \omega_{\text{th}} \tag{23}$$

the controller switches from holding to damping while inheriting the last holding MR excitation. Damping exit is evaluated by

$$\mathcal{C}_1(k) := \forall j \in \{0, 1, \ldots, N_{\text{dwell}} - 1\} : \ |\omega(k-j)| < \omega_{\text{rel}}$$
$$\mathcal{C}_2(k) := |e_\theta(k)| > \varepsilon_\theta$$
$$\mathcal{C}(k) := \mathcal{C}_1(k) \ \wedge \ \mathcal{C}_2(k). \tag{24}$$

If $\mathcal{C}(k)$ holds, guarded release and baseline recovery are executed. If $\mathcal{C}_1(k)$ holds but $\mathcal{C}_2(k)$ is false, the joint has returned to the holding window and the controller returns to holding. Thus, N_{dwell} confirms only the low-speed damping-exit/return decision in (24); holding entry remains governed by (21), and the reference-update guard in (22) remains an immediate commanded-release event.

3) Observer Gating and Mode-Wise Current Allocation: The controller uses $\hat{T}_L$ for motor feedforward and MR holding-current sizing. In MR-assisted quasi-static holding ($\omega \approx 0$), static friction and sensor noise make motion-state load updates unreliable; therefore, the observer is updated only in motion-enabled modes

$$\hat{T}_L(k^+) = \begin{cases} \text{Update}, & \sigma(k) \in \{\text{baseline}, \text{damping}\} \\ \hat{T}_L(k), & \sigma(k) = \text{holding}. \end{cases} \tag{25}$$

Freezing $\hat{T}_L$ still preserves disturbance detection because load or MR-capacity exceedance induces motion and re-enables estimation.

Given $\hat{T}_L$, the PMSM command uses $i^\star_{q,r}$ in (20), while the MR command is selected by mode and projected to actuator limits. Upon entering MR-assisted quasi-static holding, the holding target and robustness margin are computed from the recent load-estimate window $\mathcal{W}$

$$\begin{aligned} T^\star_{\text{hold}} &= \text{mean}_{k\in\mathcal{W}} \left(|\hat{T}_L(k)|\right) \\ \Delta_T &= \kappa \ \text{std}_{k\in\mathcal{W}} \left(|\hat{T}_L(k)|\right). \end{aligned} \tag{26}$$

Here, $\text{mean}_{k\in\mathcal{W}}(\cdot)$ and $\text{std}_{k\in\mathcal{W}}(\cdot)$ are statistics over $\mathcal{W}$. The buffer Δ_T covers unobserved load variation and inverse-map uncertainty within the tested range. It is not intended to compensate MR hysteresis, thermal drift, or long-term aging. The final target and coil current are

$$\begin{aligned} T_{\text{hold}} &= \Pi_{[0,\, T_{\text{MR,max}}]}\left(T^\star_{\text{hold}} + \Delta_T\right) \\ i_{\text{hold}} &= \Pi_{[0,\, i_{\text{MR,max}}]}\left(i_{\text{req}}(T_{\text{hold}})\right). \end{aligned} \tag{27}$$

The resulting compact mode-wise current policy is

$$\mathcal{U}_\sigma(x, \hat{T}_L) = \begin{cases} \begin{bmatrix} i^\star_{q,r} \\ 0 \end{bmatrix}, & \sigma = \text{baseline} \\ \begin{bmatrix} 0 \\ i_{\text{hold}} \end{bmatrix}, & \sigma = \text{holding} \\ \begin{bmatrix} i^\star_{q,r} \\ i_{\text{hold}}(k_{HD}) \end{bmatrix}, & \sigma = \text{damping} \end{cases} \tag{28}$$

where k_{HD} is the holding-to-damping transition instant. In damping, the inherited MR excitation avoids rapid remagnetization and only requires the semi-active dissipative condition $T_{\text{MR}}\omega_m \le 0$, rather than tracking a continuous MR torque reference.

During guarded release, after the nonnegative MR command reaches zero, the controller applies a short reverse-current demagnetization pulse

$$i_{\text{MR},r}(t) = \begin{cases} -i_{\text{demag}}\, \rho\left(\dfrac{t - t_R}{T_{\text{demag}}}\right), & t_R \le t < t_R + T_{\text{demag}} \\ 0, & t \ge t_R + T_{\text{demag}} \end{cases} \tag{29}$$

where $i_{\text{demag}} = 1.5$ A, $T_{\text{demag}} = 50$ ms, and $\rho(0) = \rho(1) = 0$, $\max \rho = 1$. The pulse peaks at -1.5 A and returns to zero within the release interval; it is not a sustained reverse-braking or regular torque-allocation mode.

4) Scheduler-Parameter Selection and Implementation Constraints: Scheduler parameters were selected from preliminary noise, settling, and LTO characterization and fixed for all experiments. They include holding thresholds $(\varepsilon_\theta, \varepsilon_\omega)$, reference detection $\varepsilon_{\theta r}$, velocity hysteresis $(\omega_{\text{rel}}, \omega_{\text{th}})$ with $\varepsilon_\omega < \omega_{\text{rel}} < \omega_{\text{th}}$, dwell confirmation $N_{\text{dwell}} = \lceil T_{\text{dwell}}/T_s \rceil$, and load-history margin $(\mathcal{W}, \kappa)$. These are guards and margins, not final holding-accuracy bounds; Table II lists the values.

C. Practical Stability, Hybrid Regularity, and Robustness of the Mode-Scheduled Closed Loop

1) Practical Stability Claim: This section analyzes the implemented dwell-time-constrained scheduler in terms of practical stability over the stated operating envelope. This scope is appropriate for the present semi-active MR path, whose holding action is finite-capacity, hysteretic, and saturation-limited. Let $\xi = (z, q, \chi)$, where $z = [e_\theta, \omega]^\top$, $q \in \{\text{B}, \text{H}, \text{D}, \text{R}\}$ denotes baseline, holding, damping, and guarded release, and χ collects the held load estimate, dwell counter, and release timer. The implemented scheduler is specified by the guards in (21)–(24), command projections, observer gating, and the finite-duration guarded release in (29).

Proposition: Under bounded load variation, bounded MR-map error, bounded load-estimation error, admissible command projection, and state-driven dwell confirmation, the implemented MR–motor scheduler is practically stable over the stated operating envelope. In particular, the tracking state and actuator commands remain bounded; active-mode tracking is ultimately bounded; holding is maintained only within the finite-capacity quasi-static set; low-speed exit/return events are dwell-limited; transition torques are bounded; and motor-parameter mismatch enters as a bounded perturbation.

2) Active Modes and Holding Set: For baseline and damping, the cascaded PMSM servo is represented locally as $T_e = K_p e_\theta - K_d\omega + \hat{T}_L + \delta_e$, where δ_e collects finite-bandwidth tracking, torque-constant mismatch, and unmodeled motor-side effects. With $z = [e_\theta, \omega]^\top$, the active-mode dynamics satisfy $\dot{z} = A_a z + b_a d_a$, where d_a groups load-estimation, MR-map, parameter, residual-drag, load-variation, and noise terms. Since A_a is Hurwitz for $K_p > 0$ and $K_d + B > 0$, $V_a = z^\top P z$ satisfies

$$\dot{V}_a \le -c_1|z|^2 + c_2\bar{d}_a^2 \tag{30}$$

for some $c_1, c_2 > 0$ when $|d_a| \le \bar{d}_a$; thus active-mode tracking is uniformly ultimately bounded. In damping, $T_{\text{MR}}\omega_m \le 0$, so the MR path does not inject mechanical energy.

The holding mode is represented by the finite-capacity quasi-static set

$$\begin{aligned} \Omega_{\text{hold}} = \{(e_\theta, \omega) : |e_\theta| \le \varepsilon_\theta,\ |\omega| \le \omega_{\text{th}} \\ |T_L - T_e| \le T_{\text{hold}}(i_{\text{MR}}) - \bar{\Delta}_H\} \end{aligned} \tag{31}$$

TABLE II
SCHEDULER PARAMETERS AND IMPLEMENTATION SETTINGS USED IN THE IMPLEMENTED CONTROLLER

Parameter	Role	Selection Basis/Implementation Meaning	Value
ε_θ	Holding eligibility: in-position guard	Above static/loaded positioning residuals and within the task-level holding window; not a final holding-accuracy bound.	0.1 rad rotor side; 1.58×10^{-2} rad output side
ε_ω	Holding eligibility: near-zero-speed guard	Above the static velocity-difference noise envelope.	0.12 rad/s
$\varepsilon_{\theta r}$	Reference-update detection	Separates command jitter from task-level reference changes. Once exceeded in an MR-engaged mode, it triggers guarded release before baseline tracking.	1.0×10^{-3} rad
$\omega_{\rm th}$, $\omega_{\rm rel}$	Damping entry/damping release hysteresis	$\omega_{\rm th}$ detects break-away/slip motion; $\varepsilon_\omega < \omega_{\rm rel} < \omega_{\rm th}$ forms velocity hysteresis.	0.30/0.15 rad/s
$T_{\rm dwell}$, $N_{\rm dwell}$, $f_{\rm sw,max}$	Dwell-confirmed low-speed exit/return acceptance	Rejects short velocity ripples in damping-exit/return decisions; $N_{\rm dwell} = \lceil T_{\rm dwell}/T_s \rceil$ with $f_s = 6$ kHz; $f_{\rm sw,max}$ applies to dwell-confirmed low-speed exit/return events, not to break-away entry or commanded reference-update release.	20 ms; 120 samples; $\leq 50\,{\rm s}^{-1}$
$W = \lvert\mathcal{W}\rvert$, κ	Load-history margin for holding-current allocation	Covers recent converged load estimates while avoiding stale information; κ gives a conservative margin based on recent load-estimate variation.	3000 samples (0.5 s); 3
$K_p^{\rm cmd}$, $K_\omega^{\rm cmd}$	PMSM command gains	Fixed position-command gains used by the embedded PMSM tracking loop.	5.0, 0.5
k_ω, k_T, ϕ	Saturated SMO-based LTO gains	Implementation of k_1 and k_2 in (12), with ${\rm sgn}(\omega - \hat{\omega})$ replaced by ${\rm sat}((\omega - \hat{\omega})/\phi)$ to reduce chattering.	2.0×10^3 rad/s^2; 3.0×10^2 N m/s; 0.5 rad/s
f_s, T_s	Implementation sampling	Controller, LTO, scheduler, and MR-current references are updated synchronously; the external torque sensor is used only for recording/evaluation.	6 kHz; $T_s \approx 0.167$ ms; $T_\tau = 5$ ms
f_ω, f_T	Signal filtering	First-order low-pass filters for velocity and load-torque estimate.	20/10 Hz
$T_{m,\max}^{\rm cmd}$, $i_{\rm MR,max}$, $i_{\rm demag}$	Input constraints	Motor commands are torque-projected; MR excitation is current-limited; guarded release permits only a short reverse demagnetization pulse.	22 N m; $0 \leq i_{\rm MR} \leq 1.5$ A; -1.5 A for 50 ms
$f_{\rm resp}$	Measured large-step response bandwidth	Estimated from the 10–90% rise time of loaded 5 rad rotor-side steps; distinct from the 6 kHz update rate and the dwell-limited event rate.	≈1.0 Hz

where $\bar{\Delta}_H$ bounds load-estimation, inverse-map, residual MR, and implementation uncertainties. If the margin in (26) covers these terms, the MR path balances the quasi-static load without sustained motor torque. Otherwise, induced motion violates (23) and triggers damping/release followed by active recovery. Therefore, holding is treated as finite-capacity quasi-static support, not ideal immobilization.

3) Dwell-Limited Switching and Transition Torque: The dwell-limited event-rate bound applies to dwell-confirmed low-speed damping-exit/return decisions satisfying (24). Hence

$$T_{\rm dwell} = N_{\rm dwell} T_s > 0, \qquad N_{\rm tr}(T) \leq 1 + \left\lfloor \frac{T}{T_{\rm dwell}} \right\rfloor \tag{32}$$

where $N_{\rm tr}(T)$ denotes the number of dwell-confirmed low-speed exit/return events over a finite interval of length T. Together with $\omega_{\rm rel} < \omega_{\rm th}$, this suppresses Zeno-like repeated low-speed switching and chattering in the implemented scheduler. Break-away damping entry and commanded reference-update release are handled by their guards, command projection, and finite-duration guarded release, rather than by this dwell bound.

The transition torque considered here is the joint-level resultant torque

$$T_j = T_e + T_{\rm MR} \tag{33}$$

rather than the material-level MR torque alone. Since the MR bearing switches from pre-yield holding to post-yield damping, strict C^0 or C^1 continuity of $T_{\rm MR}$ at the yield boundary is not assumed. On the projected operating domain, $T_e = K_t i_q$ and the identified MR maps have finite local slopes. Thus, within a fixed mode σ

$$|\Delta T_j| \leq K_t |\Delta i_q| + L_{\sigma,i} |\Delta i_{\rm MR}| + L_{\sigma,\nu} |\Delta \nu| \tag{34}$$

where $\nu = |\omega_m|$, and $L_{\sigma,i}$ and $L_{\sigma,\nu}$ are finite local slope bounds. At holding-to-damping switching, the damping mode inherits the latest holding current

$$i_{{\rm MR},r}(k_{\rm HD}^+) = i_{{\rm MR},r}(k_{\rm HD}^-) = i_{\rm hold}(k_{\rm HD}^-) \tag{35}$$

so the scheduler introduces no additional MR-current command jump. The remaining static-to-dynamic jump is conservatively bounded by

$$\begin{aligned} |\Delta_J T_j^{\rm HD}| \leq{}& K_t |\Delta_J i_q| + T_{\rm hold}(i_{\rm hold}) \\ &+ F_{\rm MR}(i_{\rm hold}, |\omega_{\rm sw}|) + \Delta T_{\rm id} \end{aligned} \tag{36}$$

where $\Delta_J(\cdot)$ denotes the jump across the switching instant, $\omega_{\rm sw}$ is the switching speed, and $\Delta T_{\rm id}$ bounds the static/dynamic MR-map identification errors. Combining (34)–(36) with (32), T_j is piecewise increment-constrained and has only finitely many bounded switching jumps over finite horizons. During guarded release, the finite pulse satisfies $|i_{{\rm MR},r}| \leq i_{\rm demag} = 1.5$ A over $T_{\rm demag} = 50$ ms; hence the release-induced torque is bounded before motor-dominated recovery resumes.

4) Parameter-Mismatch Propagation: Motor-parameter mismatch enlarges the practical bounds through the SMO-based load-torque observer and feedforward channel. With $J_c = J(1+\delta_J)$, $B_c = B(1+\delta_B)$, and $K_{t,c} = K_t(1+\delta_K)$, the dominant mismatch-induced load-estimate component is

$$e_T^p \approx -\Delta J \dot{\omega} + \Delta T_e - \Delta B \omega \tag{37}$$

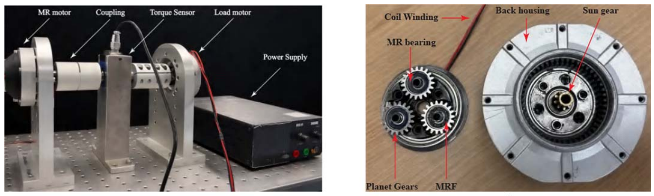

(a) (b)

Fig. 3. Experimental platform and MR-motor joint prototype. (a) Testbed. (b) Prototype.

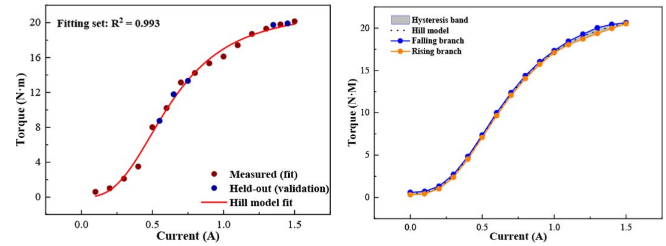

(a) (b)

Fig. 4. Static and quasi-static MR torque characterization: (a) holding fit; and (b) quasi-static hysteresis.

where $\Delta J = J_c - J$, $\Delta B = B_c - B$, and $\Delta T_e = (K_{t,c} - K_t)i_q$. Inertia/damping mismatch mainly affects transients; torque-constant mismatch scales feedforward as $i^{\rm ff}_{q,r} = (1+\delta_K)^{-1}\hat{T}_L/K_t$, with the resulting motor command bounded by the torque-command projection $|T_m^{\rm cmd}| \le 22\,{\rm N\cdot m}$. Load-estimation bias may shift switching instants or enlarge transient bounds, but guards still use measured e_θ, ω, and $\Delta\theta_{\rm ref}$ with projection, state-driven dwell confirmation, and break-away recovery. If load or parameter drift is excessive, the guarantee reduces to guarded exit and active recovery.

IV. Experimental Studies

This section validates the proposed load-aware mode-scheduled coordination framework via hardware experiments on an integrated MR–motor prototype (Fig. 3). The experiments are organized into five parts:

1) MR torque characterization and hysteresis evaluation for the holding and post-yield resistive maps.
2) SMO-based load-torque observer validation under stepwise disturbances.
3) near-rated constant-load quasi-static holding to evaluate energy saving, holding error, drift, and fixed-current MR ablations.
4) an application-inspired variable-load tracking-and-holding task to assess disturbance attenuation, repeated release/re-engagement, and energy use.
5) motor-parameter sensitivity evaluation under representative J, B, and K_t mismatch.

All applied load changes are finite-slew actuator-generated transitions interpreted from the measured load-torque trace; successful trials complete the prescribed holding/release/recovery sequence without unresolved break-away or safety-supervisor interruption, and residual behavior is quantified by the reported error and drift metrics.

A. MR Torque Characterization and Model Identification

This section identifies the static holding-limit model $T_{\rm hold}(i_{\rm MR})$ in (2) and the post-yield resistive surface $\mathcal{F}_{\rm MR}(i_{\rm MR}, |\omega_m|)$ in (5) and (6). The static/quasi-static characterization, dynamic-slip validation, and identified parameters are summarized in Figs. 4, 5, and Table III.

1) Holding Model Identification and Validation: The static holding capacity was measured by a quasi-static torque ramp at near-zero slip. Currents $i_{\rm MR} \in [0.1,\ 1.5]$ A with $\Delta i_{\rm MR} = 0.1$ A were used for identification, and $\{0.55, 0.65, 0.75, 1.35, 1.45\}$ A were held out for validation. As shown in Fig. 4(a), the forward model achieves $R^2_{\rm val} = 0.991$ and ${\rm RMSE_{val}} = 0.425$ N·m on held-out samples; inverse-map round-trip validation gives ${\rm RMSE}_i = 0.0286$ A and $\max|\Delta i| = 0.0414$ A.

2) Quasi-Static Holding Hysteresis Characterization: The MR current was swept from 0 to 1.5 A and back to 0 A under near-zero slip. As shown in Fig. 4(b), the falling branch is slightly higher than the rising branch; the maximum rise–fall mismatch is 0.686 N·m at $i_{\rm MR} = 1.3$ A, or 3.07% of the identified saturation torque. Thus, the static map is used as a control-oriented nominal holding-capacity map, and insufficient holding caused by hysteresis or map mismatch is exposed as slip/position deviation that triggers PMSM-dominated recovery.

3) Dynamic Slip Mapping and Surface Validation: Dynamic-slip data were collected over $i_{\rm MR} \in [0,\ 1.5]$ A and $|\omega_m| \in [0.5,\ 10]$ rad/s, with held-out current slices (0.7, 1.4 A) and speed slices (0.25, 9.5 rad/s) for validation. The fitted surface and validation slices are shown in Fig. 5, and the identified parameters are listed in Table III. The identification achieves $R^2_{\rm hold} = 0.993$ and $R^2_{\rm dyn} = 0.9986$.

B. Validation of Load Torque Observer

To assess the dynamic tracking capability of the proposed SMO under practical operating conditions, experiments are conducted during the position-holding phase. In this scenario, the rotor position is regulated by a closed-loop position controller, while an external load torque is abruptly applied to the output shaft. The observer estimates the load torque online based on the measured electrical and mechanical states.

Fig. 6 depicts the estimation results under three distinct load levels: $T_L = 2.6$, 5.3, and $9.2\,{\rm N\cdot m}$. The upper panels compare the estimated load torque $\hat{T}_L$ with the actual applied torque measured by the reference sensor, while the lower panels quantify the estimation error. At $t = 0$, a step load disturbance is applied, triggering the observer's transient response.

For the low-load case ($T_L = 2.6\,{\rm N\cdot m}$), the estimated torque rapidly converges to the actual value with a settling time of approximately $0.057\,{\rm s}$, maintaining a steady-state error within $\pm 0.15\,{\rm N\cdot m}$. As the load magnitude increases to $5.3\,{\rm N\cdot m}$, the convergence time rises slightly to $0.098\,{\rm s}$, with the error bound remaining within $\pm 0.30\,{\rm N\cdot m}$. Under the highest tested load

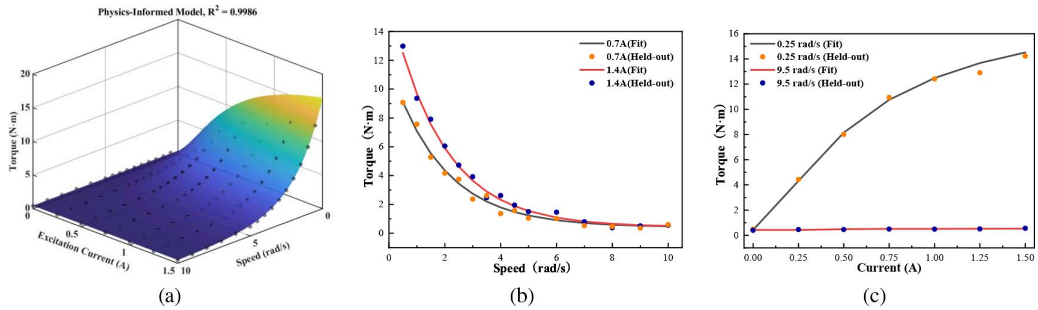

Fig. 5. Dynamic resistive MR torque characterization and validation: (a) post-yield torque surface; (b) held-out current-slice validation; and (c) held-out speed-slice validation.

TABLE III
IDENTIFIED MR TORQUE-MODEL PARAMETERS

Static Par.	Value	Unit	Dynamic Par.	Value	Unit
T_{sat}	22.3239	N·m	T'_{sat}	20.31	N·m
T_{res}	0.428018	N·m	T'_{res}	0.4264	N·m
n	2.79539	–	n'	1.454	–
k	0.673665	A	k'	0.5994	A
–	–	–	λ	0.53	s/rad

of $9.2\,\text{N}\cdot\text{m}$, the observer continues to converge reliably with a settling time of $0.253\,\text{s}$ and a bounded error of $\pm 0.56\,\text{N}\cdot\text{m}$.

These results indicate that, within the tested load range, the proposed observer provides bounded load-torque estimates with convergence times and error envelopes suitable for the subsequent cooperative control.

C. Energy-Efficient Near-Rated High-Load Quasi-Static Holding via Mode-Scheduled MR Assistance

Constant-load holding was tested at $T_L \in \{10, 15, 20\}\,\text{N}\cdot\text{m}$ using PMSM-only active holding, scheduled fixed-current MR holding at $0.75/1.5\,\text{A}$, and the proposed load-aware MR excitation from $\hat{T}_L$. The fixed-current cases retain the same holding-entry/release sequence but replace load-aware sizing with constant excitation; hence they ablate current sizing under the same scheduled holding/release protocol, not the scheduler alone.

In Fig. 7, shaded intervals are motion/observation windows where the SMO-based LTO updates $\hat{T}_L$; unshaded intervals are quasi-static holding windows in which the latest converged load estimate is held for MR-current allocation.

The holding state is evaluated as a pre-yield MR process using the absolute holding error and residual drift

$$e_{\text{ss}}^{\max} = \max_{t \in \mathcal{T}_h} |\theta(t) - \theta_{\text{ref}}(t)|, \qquad D_{\max} = \max_{t \in \mathcal{T}_h} |\theta(t) - \theta_0| \tag{38}$$

where $\mathcal{T}_h$ is the evaluated steady holding window and $\theta_0 = \theta(t_0)$ is the post-switching rotor position. A failure is declared when the tolerance band cannot be maintained, and the safety supervisor is triggered; the following recovery interval is excluded.

As shown in Fig. 7 and Table IV, the proposed method succeeds under all tested loads. At $20\,\text{N}\cdot\text{m}$, $\bar{P}_{\text{tot}}$ decreases by 87.3% (246.43 to 31.39 W), with $e_{\text{ss}}^{\max} < 3.7 \times 10^{-2}\,\text{rad}$ and $D_{\max} \leq 1.0 \times 10^{-3}\,\text{rad}$. The $20\,\text{N}\cdot\text{m}$ case corresponds to 90.9% of the $22\,\text{N}\cdot\text{m}$ output torque limit in Table I, extending the validation to a high-load condition close to the actuator limit.

The fixed-current cases isolate the effect of load-aware current allocation. They use the same MR hardware and the same holding/release sequence, but replace observer-based current sizing with constant MR excitation. Fixed $0.75\,\text{A}$ fails at 15 and $20\,\text{N}\cdot\text{m}$ because of insufficient holding capacity, whereas fixed $1.5\,\text{A}$ and the proposed method both succeed through the same finite-capacity quasi-static holding mechanism. Compared with fixed $1.5\,\text{A}$, the proposed allocation reduces accounted total power by 51.3% and 25.0% at 10 and $15\,\text{N}\cdot\text{m}$, respectively, while maintaining comparable holding error and drift; at $20\,\text{N}\cdot\text{m}$, the required capacity approaches MR saturation, so the proposed current and power naturally approach the fixed high-current case.

Here, $D_{\max}$ quantifies finite-window drift, not indefinite immobilization; macroscopic break-away triggers damping/release and motor recovery.

D. Application-Inspired Variable-Load Tracking-and-Holding Task for Disturbance and Energy Evaluation

A $30\,\text{s}$ variable-load tracking-and-holding task is conducted on the torque test platform to emulate representative load-varying position-control episodes of robotic manipulator joints, including loaded transfers, target holding, load increase/decrease, bounded fluctuations, and guarded MR release/re-engagement. This task evaluates disturbance attenuation and energy use under repeated reference and output-side load variations.

Five cases were compared: G1, motor-only PD; G2, motor-only LTO-AC with $\hat{T}_L$ feedforward and $i_{\text{MR}} = 0$; G3/G4, scheduled fixed-current MR baselines at $0.75/1.5\,\text{A}$; and G5, the proposed load-aware hybrid coordination. Hierarchically, G1/G2 evaluate motor-only compensation, G3/G4 retain the scheduled MR engagement/release protocol but use constant excitation to isolate current sizing, and G2 versus G5 evaluates the integrated benefit of a scheduled MR branch with load-aware sizing.

Robust or optimal motor-side controllers can improve active disturbance rejection but still require continuous electromagnetic torque during static holding. Accordingly, LTO-AC is the

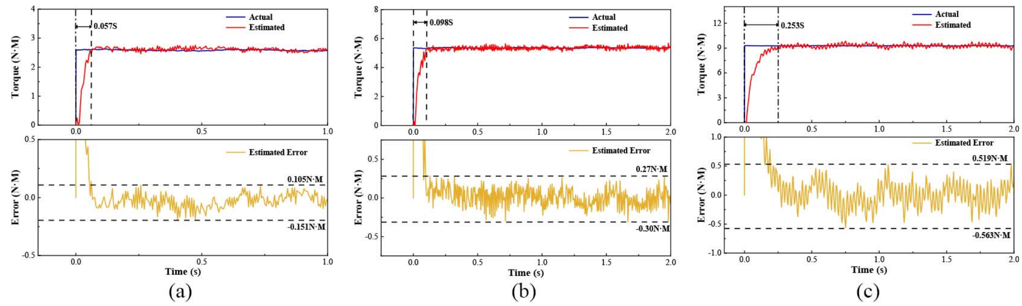

Fig. 6. Load-torque observer response to step loads: measured/estimated torque and error. (a) $T_L = 2.6$ N·m. (b) $T_L = 5.3$ N·m. (c) $T_L = 9.2$ N·m.

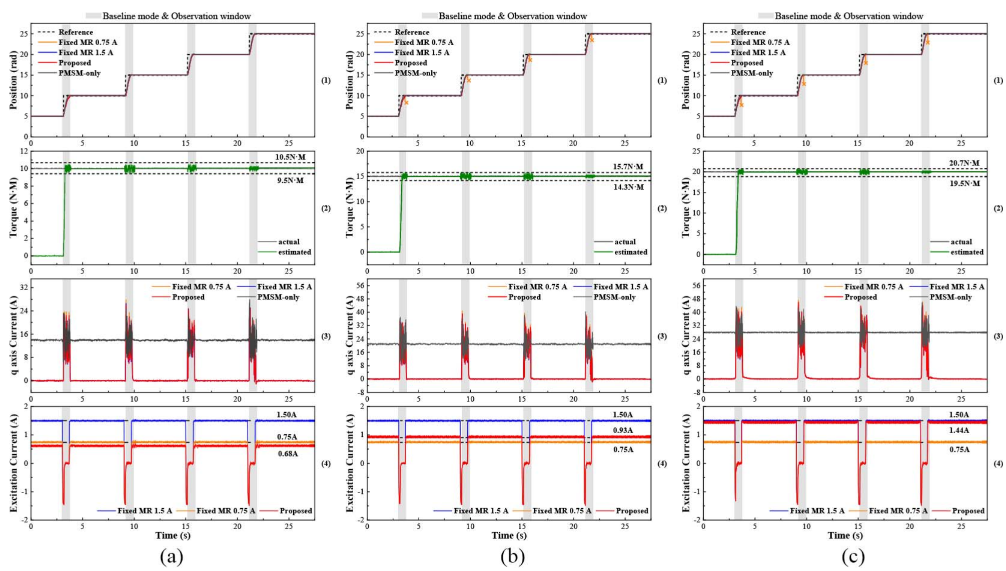

Fig. 7. Near-rated quasi-static holding. Shaded regions denote motion/observation; negative-current segments are guarded-release pulses (29); crosses mark fixed-current failures excluded from statistics. (a) $T_L = 10$ N·m. (b) $T_L = 15$ N·m. (c) $T_L = 20$ N·m.

TABLE IV
HIGH-LOAD HOLDING PERFORMANCE AND SEQUENCE-AVERAGED POWER

Load (N·m)	Method	Res.	$\bar{P}_m$ (W)	$\bar{P}_c$ (W)	$\bar{P}_{\rm tot}$ (W)	Save (%)	$e_{\rm rms}$ (mrad)	$e_{\max}$ (mrad)	$D_{\max}$ (mrad)
10	PMSM	A	61.91	0	61.91	–	23.2	33.5	–
10	Fix 0.75 A	S	6.22	2.69	8.90	85.6	24.1	35.8	≤ 1.0
10	Fix 1.5 A	S	5.76	10.29	16.05	74.1	24.6	36.6	≤ 1.0
10	Prop.	S	5.96	1.87	7.82	87.4	23.9	35.1	≤ 1.0
15	PMSM	A	139.30	0	139.30	–	28.2	40.5	–
15	Fix 0.75 A	F	–	–	–	–	–	–	–
15	Fix 1.5 A	S	12.72	10.29	23.01	83.5	24.7	36.8	≤ 1.0
15	Prop.	S	13.20	4.06	17.26	87.6	24.2	35.7	≤ 1.0
20	PMSM	A	246.43	0	246.43	–	23.5	34.6	–
20	Fix 0.75 A	F	–	–	–	–	–	–	–
20	Fix 1.5 A	S	21.15	10.30	31.45	87.2	20.8	30.9	≤ 1.0
20	Prop.	S	21.83	9.56	31.39	87.3	24.3	36.1	≤ 1.0

Note: PMSM: active holding; Fix: fixed MR current; Prop.: load-aware allocation. A/S/F denote active, successful MR holding, and failure. Power values are complete 25-s sequence averages; $\bar{P}_{\rm tot} = \bar{P}_m + \bar{P}_c$. Failed cases are not evaluated. Errors are rotor-side; output-side values equal rotor-side values divided by $N_g = 6.33$.

motor-only reference, G3/G4 are current-sizing ablations under scheduled MR engagement, and G5 is the full coordination case.

Fig. 8 shows representative responses for G2, G3, and G5, with all metrics in Table VI. G5 reduces load-increase deviations relative to G2/G3; when load decreases within MR capacity, pre-yield holding sustains the new load without visible excursion, consistent with holding $\hat{T}_L$ during quasi-static holding.

Fig. 9 confirms that G5 reduces a representative high-load deviation relative to LTO-AC and Fixed-0.75A MR. The short negative pulse is only for guarded demagnetization; the MR path is removed before motor-dominated recovery and re-engaged after quasi-static holding resumes.

For quantitative evaluation, peak disturbance error excludes planned tracking transients over $\mathcal{T}_{\rm hd} = [0, 1.5] \cup [3.5, 7.0] \cup [9.0, 15.0] \cup [17.0, 22.0] \cup [24.0, 30.0]$ s, while rms error and IAE use $[0, T]$

$$e_{\max} = \max_{t \in \mathcal{T}_{\rm hd}} |e_\theta(t)|, \quad e_{\rm rms} = \sqrt{\frac{1}{T}\int_0^T e_\theta^2(t)\,dt}$$
$$J_{\rm IAE} = \int_0^T |e_\theta(t)|\,dt. \tag{39}$$

TABLE V
COMPACT PROTOCOL SUMMARY OF THE VARIABLE-LOAD TRACKING-AND-HOLDING TASK

Phase	Time (s)	Position Reference (Rotor Side)	Output-Side Load Command	Purpose/Rate Information
P1	0–3.5	hold 0 rad, then smooth $0 \rightarrow 5$ rad	$8\ \mathrm{N \cdot m}$	initial holding and planned approach
P2	3.5–7.0	hold 5 rad	$8\ \mathrm{N \cdot m}$, then $6 + 2\sin(2\pi \cdot 0.5(t-5.0))\ \ \mathrm{N \cdot m}$	low-load holding and fluctuation; $\lvert \dot{T}_L \rvert_{\max} = 6.28\ \mathrm{N \cdot m/s}$
P3	7.0–15.0	smooth $5 \rightarrow 2$ rad, then hold 2 rad	$2\ \mathrm{N \cdot m}$ during motion; then $2 \rightarrow 6 \rightarrow 2 \rightarrow 10\ \mathrm{N \cdot m}$ with 1.5 s plateaus	low-/medium-load steps; rate from measured T_L
P4	15.0–17.0	smooth $2 \rightarrow -0.5$ rad	$10\ \mathrm{N \cdot m}$	loaded planned transfer
P5	17.0–22.0	hold -0.5 rad	$10 \rightarrow 18\ \mathrm{N \cdot m}$, then $15 + 3\sin(2\pi \cdot 0.5(t-20.0))\ \ \mathrm{N \cdot m}$	high-load step loading and fluctuation; $\lvert \dot{T}_L \rvert_{\max} = 9.42\ \mathrm{N \cdot m/s}$
P6	22.0–24.0	smooth $-0.5 \rightarrow 1$ rad	$12\ \mathrm{N \cdot m}$	loaded planned transfer
P7	24.0–30.0	hold 1 rad	$12 \rightarrow 16 \rightarrow 12 \rightarrow 20\ \mathrm{N \cdot m}$ with 1.5 s plateaus	high-load steps and short challenge; rate from measured T_L

Note: For step-load phases, the command is piecewise constant and changes at the phase boundary. The actual load-transition rate is actuator-limited and is evaluated from the measured output-side torque as $r_L^{10-90} = \lvert \Delta T_L \rvert / t_{10-90}^{\mathrm{meas}}$. Planned position-transition intervals are excluded from the peak disturbance-error evaluation.

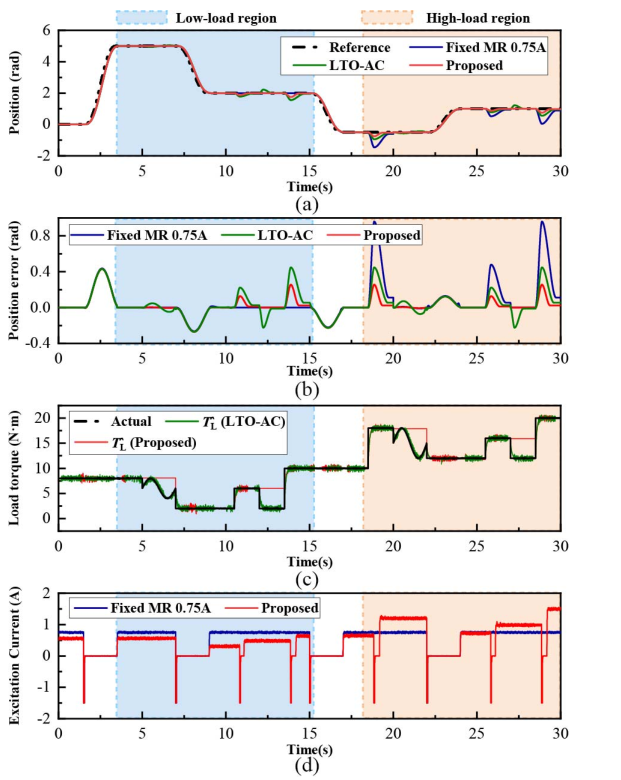

Fig. 8. Variable-load tracking-and-holding task: (a) rotor-side position; (b) rotor-side error; (c) measured/estimated output-side load torque; and (d) MR current. Shaded regions follow Table V.

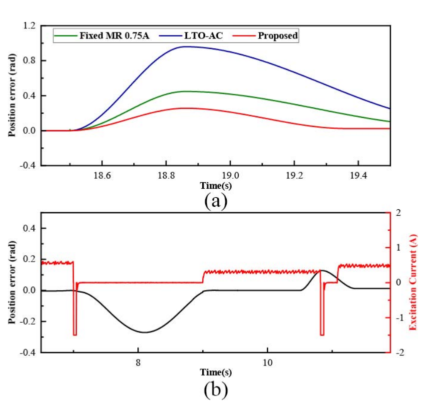

Fig. 9. Magnified high-load disturbance and guarded-release response.

TABLE VI
QUANTITATIVE COMPARISON IN THE VARIABLE-LOAD TRACKING-AND-HOLDING TASK

Method	$e_{\max}$ (rad)	e_{RMS} (rad)	J_{IAE} (rad·s)	$\bar{P}_{\mathrm{motor}}$ (W)	$\bar{P}_{\mathrm{MR}}$ (W)	$\bar{P}_{\mathrm{total}}$ (W)
Motor-only PD	1.2041	0.3062	5.2205	157.596	0.000	157.596
LTO-AC	0.4480	0.1439	2.6472	115.327	0.000	115.327
Fixed-0.75A MR	0.9605	0.2062	2.8073	62.866	2.056	64.923
Fixed-1.5A MR	0.0173	0.0943	1.1818	20.819	8.228	29.046
Proposed	0.2560	0.1068	1.6649	22.423	2.138	24.561

Note: Error metrics are evaluated from rotor-side position signals; load torques are output-side quantities.

The motor copper loss, MR-coil Joule loss, and accounted total average power are evaluated from measured currents using the same resistance-based accounting. For the variable-load task, these quantities are reported as $\bar{P}_{\mathrm{motor}}$, $\bar{P}_{\mathrm{MR}}$, and $\bar{P}_{\mathrm{total}} = \bar{P}_{\mathrm{motor}} + \bar{P}_{\mathrm{MR}}$ for all compared methods.

Table VI summarizes the metrics. Compared with G1, G2 reduces J_{IAE} from 5.2205 to 2.6472 $\mathrm{rad \cdot s}$ and $\bar{P}_{\mathrm{total}}$ from 157.596 to 115.327 W, confirming the benefit of motor-side load-torque compensation. The G2-to-G5 comparison evaluates the complete MR-assisted coordination: scheduled engagement, guarded release/re-engagement, and load-aware sizing. Relative to G2, G5 reduces $e_{\max}$ from 0.4480 to 0.2560 rad and accounted total average power from 115.327 to 24.561 W; motor-side compensation alone therefore cannot remove the continuous holding burden.

Fixed-current MR baselines isolate the current-sizing benefit. G3 saves power but lacks high-load margin ($e_{\max} = 0.9605$ rad), whereas G4 gives the smallest errors by conservative excitation but uses 8.228 W average MR-coil power. G5 does not minimize all errors; relative to G4, it reduces MR-coil power from 8.228 to 2.138 W and accounted total average power from 29.046 to 24.561 W. Thus, G3/G4 versus G5 quantifies current sizing, while the variable-load task functionally validates role scheduling through planned release, holding, break-away response, recovery, and re-engagement; no separate percentage contribution is assigned to the scheduler alone.

E. Motor-Parameter Sensitivity Evaluation

The MR–motor prototype and load remain unchanged; only the nominal parameters in the SMO-based LTO and command

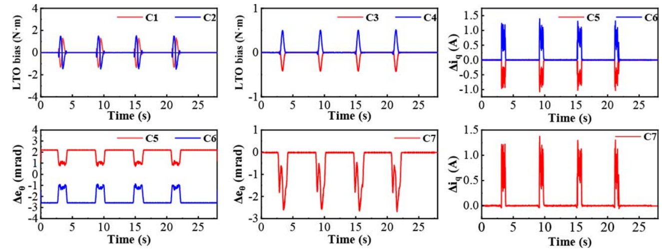

Fig. 10. Motor-parameter sensitivity at $10\,\mathrm{N\cdot m}$. C1/C2: $J_c = 1.1J/0.9J$; C3/C4: $B_c = 1.2B/0.8B$; C5/C6: $K_{t,c} = 1.05K_t/0.95K_t$; C7: $J_c = 0.9J$, $B_c = 0.8B$, $K_{t,c} = 0.95K_t$. Δe_θ and Δi_q are relative to C0.

law are perturbed to emulate controller-side mismatch. Sensitivity to nominal motor-parameter mismatch was evaluated under the same $10\,\mathrm{N\cdot m}$ condition as Fig. 7(a).

Seven cases were considered: nominal C0; inertia mismatch C1/C2; damping mismatch C3/C4; torque-constant mismatch C5/C6; and combined mismatch C7, with perturbations listed in Fig. 10. The tracking-error and q-axis-current differences are defined relative to C0 as

$$\Delta e_\theta = e_{\theta,\mathrm{case}} - e_{\theta,\mathrm{C0}}, \qquad \Delta i_q = i_{q,\mathrm{case}} - i_{q,\mathrm{C0}}. \tag{40}$$

Fig. 10 shows that inertia/damping mismatch mainly affects LTO transients, whereas torque-constant mismatch appears in the torque-current channel. In the adverse case C7, the maximum LTO bias, baseline-corrected tracking-error variation, and additional q-axis current are $1.536\,\mathrm{N\,m}$, $2.691\,\mathrm{mrad}$, and $1.375\,\mathrm{A}$, respectively. The MR-current command changes negligibly in these controller-side mismatch tests, and no unrecoverable tracking failure or additional mode switching is observed. These results indicate bounded sensitivity within the tested mismatch range. They should not be interpreted as robustness to arbitrary plant changes, hardware replacement, or long-term parameter drift, for which recalibration or online adaptation would be required.

V. Conclusion

This article presented a joint-level coordination framework for an MR-assisted PMSM joint that preserves a standard position-reference interface while coordinating low-drag tracking, finite-capacity MR-assisted holding, post-yield damping, and guarded release inside the joint module. Experiments on the integrated prototype verify reduced holding power and an improved disturbance-response/energy trade-off compared with motor-only and fixed-current MR baselines. These results indicate that the improvement mainly arises from load-aware MR-path scheduling and current allocation, rather than from the MR hardware alone.

For long-duration deployment, the identified MR maps should be treated as nominal because hysteresis, thermal effects, wear, aging, and MR-medium creep may shift the holding capacity and resistive torque. Future work will address robotic-platform validation, rapidly varying loads, temperature-aware MR-map adaptation, online recalibration, creep characterization, and drive-level current shaping.

References

[1] S. Li, Y. Xu, W. Zhang, and J. Zou, "A novel two-phase mode switching control strategy for pmsm position servo systems with fast-response and high-precision," *IEEE Trans. Power Electron.*, vol. 38, no. 1, pp. 803–815, Jan. 2023.

[2] L. Chen, H. Zhang, H. Wang, K. Shao, G. Wang, and A. Yazdani, "Continuous adaptive fast terminal sliding mode-based speed regulation control of PMSM drive via improved super-twisting observer," *IEEE Trans. Ind. Electron.*, vol. 71, no. 5, pp. 5105–5115, May 2024.

[3] W. Ding, L. Huo, and S. Chen, "Disturbance observer-based active damping control for electrolytic capacitor-less PMSM drives," *IEEE Trans. Ind. Electron.*, vol. 71, no. 12, pp. 15383–15392, Dec. 2024.

[4] A. St-Jean, F. Dorval, J.-S. Plante, and A. Lussier-Desbiens, "Magnetorheological-actuators: An enabling technology for fast, safe, and practical collaborative robots," *IEEE Trans. Robot.*, vol. 40, pp. 1261–1272, 2024.

[5] R. F. A. Khan, K. Rsetam, Z. Cao, and Z. Man, "Singular perturbation-based adaptive integral sliding mode control for flexible joint robots," *IEEE Trans. Ind. Electron.*, vol. 70, no. 10, pp. 10516–10525, Oct. 2023.

[6] T. Wang, Y. Liu, W. Xia, and C. Liu, "Design and control of a multimodal compliant actuator based on a scissor-epicyclic mechanism for wearable robotics," *IEEE Trans. Ind. Electron.*, vol. 72, no. 7, pp. 7329–7342, Jul. 2025.

[7] H. Fan, H. Wei, D. Xu, and Y. Liu, "Closed-loop iterative optimized fractional-order PID current control of PMSM," *IEEE Trans. Ind. Informat.*, vol. 21, no. 2, pp. 1120–1129, Feb. 2025.

[8] M. Gadaleta, M. Pellicciari, and G. Berselli, "Optimization of the energy consumption of industrial robots for automatic code generation," *Rob. Comput. Integr. Manuf.*, vol. 57, no. 3, pp. 452–464, 2019. [Online]. Available: https://www.sciencedirect.com/science/article/pii/S0736584518301856

[9] B. Vanderborght et al., "Variable impedance actuators: A review," *Rob. Auton. Syst.*, vol. 61, no. 12, pp. 1601–1614, 2013. [Online]. Available: https://www.sciencedirect.com/science/article/pii/S0921889013001188

[10] C. Véronneau et al., "Modular magnetorheological actuator with high torque density and transparency for the collaborative robot industry," *IEEE Robot. Automat. Lett.*, vol. 8, no. 2, pp. 896–903, Feb. 2023.

[11] J. R. Morillas and J. de Vicente, "Magnetorheology: A review," *Soft Matter*, vol. 16, pp. 9614–9642, 2020.

[12] J. Wu, W. Kong, and Y. Liu, "Structural development of magnetorheological fluid brakes/clutches as typical transmission devices: A review," *J. Magn. Magn. Mater.*, vol. 614, 2025, Art. no. 172697.

[13] D. Chen, Y. Fang, H. Ni, Y. Zhang, J. Liu, and A. Song, "Development of a small rotary MR brake working in mixed mode for haptic applications," *IEEE Trans. Instrum. Meas.*, vol. 73, pp. 1–12, 2024.

[14] S. Pisetskiy and M. R. Kermani, "A concept of a miniaturized MR clutch utilizing MR fluid in squeeze mode," in *Proc. IEEE/RSJ Int. Conf. Intell. Robots Syst. (IROS).* Piscataway, NJ, USA: IEEE Press, 2020, pp. 6347–6352.

[15] A. Singh, M. Kumar Thakur, and C. Sarkar, "Design and development of a wedge-shaped magnetorheological clutch," *Proc. Inst. Mech. Engineers, Part L: J. Materials: Des. Appl.*, vol. 234, no. 9, pp. 1252–1266, 2020.

[16] M. Plooij, G. Mathijssen, P. Cherelle, D. Lefeber, and B. Vanderborght, "Lock your robot: A review of locking devices in robotics," *IEEE Robot. Automat. Mag.*, vol. 22, no. 1, pp. 106–117, Jan. 2015.

[17] D. Shin, A. Tanaka, N. Kim, and O. Khatib, "A centrifugal force-based, configuration-independent, high-torque-density, passive brake for human-friendly robots," *IEEE/ASME Trans. Mechatron.*, vol. 21, no. 6, pp. 2827–2835, Jun. 2016.

[18] S. Yu et al., "Quasi-direct drive actuation for a lightweight hip exoskeleton with high backdrivability and high bandwidth," *IEEE/ASME Trans. Mechatron.*, vol. 25, no. 4, pp. 1794–1802, Aug. 2020.

[19] J. Zhu, C. Jiao, I. Dominguez, S. Yu, and H. Su, "Design and backdrivability modeling of a portable high torque robotic knee prosthesis with intrinsic compliance for agile activities," *IEEE/ASME Trans. Mechatron.*, vol. 27, no. 4, pp. 1837–1845, Apr. 2022.

[20] H. Ochoa and R. Cortesão, "Impedance control architecture for robotic-assisted mold polishing based on human demonstration," *IEEE Trans. Ind. Electron.*, vol. 69, no. 4, pp. 3822–3830, Apr. 2022.

[21] B. Zhou, Y. Sun, W. Liu, and S. Li, "Active admittance control with iterative learning for general-purpose contact-rich manipulation," *IEEE Trans. Ind. Electron.*, vol. 72, no. 3, pp. 2842–2851, Mar. 2025.

[22] D. Hua, X. Liu, Z. Li, P. Fracz, A. Hnydiuk-Stefan, and Z. Li, "A review on structural configurations of magnetorheological fluid-based devices reported in 2018–2020," *Front. Mater.*, vol. 8, 2021, Art. no. 640102. [Online]. Available: https://www.frontiersin.org/journals/materials/articles/10.3389/fmats.2021

[23] H. Qin, A. Song, and Y. Mo, "A hybrid actuator with hollowed multi-drum magnetorheological brake and direct-current micromotor for hysteresis compensation," *J. Intell. Mater. Syst. Struct.*, vol. 30, no. 7, pp. 1031–1042, 2019. [Online]. Available: https://doi.org/10.1177/1045389X19828473

[24] J. Zhao et al., "Modeling and torque control against rate-dependent hysteresis of a magnetorheological fluid dual clutch in an electric vehicle transmission system," *IEEE/ASME Trans. Mechatron.*, vol. 30, no. 1, pp. 27–37, Jan. 2025.

[25] Q. Shi et al., "Design and testing of magnetorheological brake with adjustable interdigitated combs for lower limb prostheses and exoskeletons," *Smart Mater. Struct.*, vol. 34, no. 5, 2025.

[26] J. Di Carlo, P. M. Wensing, B. Katz, G. Bledt, and S. Kim, "Dynamic locomotion in the MIT cheetah 3 through convex model-predictive control," in *Proc. IEEE/RSJ Int. Conf. Intell. Robots Syst. (IROS)*. Piscataway, NJ, USA: IEEE Press, 2018, pp. 1–9.

[27] C. D. Bellicoso, F. Jenelten, C. Gehring, and M. Hutter, "Dynamic locomotion through online nonlinear motion predictive control," *IEEE Robot. Automat. Lett.*, vol. 3, no. 3, pp. 2261–2268, Mar. 2018.

[28] D. J. Braun, M. Howard, and S. Vijayakumar, "Optimal variable stiffness control: Formulation and application to explosive movement tasks," *Auton. Robots*, vol. 33, no. 3, pp. 237–253, 2012.

[29] E. A. T. Yew et al., "MR_Go: A magnetorheological quadruped robot for energy-efficient, high-payload, and impact-tolerant planetary exploration," *IEEE Robot. Automat. Lett.*, vol. 11, no. 5, pp. 5670–5677, May 2026.

[30] Y. Miao, H. Ge, M. Preindl, J. Ye, B. Cheng, and A. Emadi, "MTPA fitting and torque estimation technique based on a new flux-linkage model for interior-permanent-magnet synchronous machines," *IEEE Trans. Ind. Appl.*, vol. 53, no. 6, pp. 5451–5460, Jun. 2017.

Zirui Chen received the B.S. degree in automation from Anhui University, Anhui, China, in 2024. He is currently working toward the M.S. degree in control engineering with the University of Science and Technology of China, Hefei, China.

His research interests include mechatronic design for robotic joints, control algorithms, and embedded electronic system design.

Erwin Ang Tien Yew received the M.S. degree in mechanical engineering/mechatronics from the University of Southampton, Southampton, U.K., in 2022. He is currently working toward the Ph.D. degree in biological engineering mechanics with the School of Engineering Sciences, University of Science and Technology of China, Hefei, China.

His research interests include quadruped robot control systems and the design of magnetorheological actuator systems, specifically for robotic actuation.

Yuekang Fu received the B.E. degree in control engineering from the Northeastern University, Qinhuangdao, China, in 2025. He is currently working toward the Ph.D. degree in engineering with the University of Science and Technology of China, Hefei, China.

His research interests include magnetorheological actuators, upper-limb robotic arms based on magnetorheological actuators, robot design and control, as well as system modeling.

Zhongyuan Kong received the B.S. degree in automation from Anhui University, Anhui, China, in 2024. He is currently working toward the master's degree in instrumentation engineering with the School of Engineering Science, University of Science and Technology of China, Hefei, China.

His research interests include MR damper-based actuation, human–robot collaboration, and teleoperation force feedback.

Liang Zhang (Member, IEEE) received the B.Eng. degree in automation from Shandong University, Jinan, China, in 2015, and the Ph.D. degree in aeronautical and astronautical science and technology from the School of Astronautics, Harbin Institute of Technology, Harbin, China, in 2021.

From 2018 to 2019, he was also a visiting Ph.D. Student with the Autonomous System Laboratory, ETH Zurich, Switzerland, under the foundation of the China Scholarship Council. He is currently an Associate Professor with the School of Electrical Engineering and Automation, Anhui University, Anhui, China. His research interests include mainly around the multirobot or multiagent system (MAS/MRS), including distributed estimation, cooperative control, and planning under uncertainty.

Shuaishuai Sun received the B.E. degree in mechanical engineering and automation from China University of Mining and Technology, Beijing, China, in 2011, and the Ph.D. degree in mechanical engineering from the University of Wollongong, NSW, Australia, in 2016.

He worked as a Postdoctoral Researcher with the University of Wollongong and an Assistant Professor with Tohoku University, Sendai, Japan. He is currently working as a Professor with the Department of Precision Machinery and Precision Instrumentation, University of Science and Technology of China (USTC), Hefei, China. His research interests include intelligent mechanical and mechatronic systems, system dynamics, smart materials and structures, innovative actuators for locomotive robots, and vibration control.

Dr. Sun has published more than 120 journal articles in his research field and serves as an Associate Editor or Academic Editor for several journals.